energies

MDPI

Article

Novel Multi-Physics Computational Simulation of a 10 kW Permanent Magnet Motor for Podded Propulsion

Jang-Hyun Park [1,2], Tae-Woo Lee [2], Yeon-Ho Jeong [2] and Do-Kwan Hong [1,2,*]

[1] Electric Energy Conversion Engineering, University of Science and Technology, Changwon 51543, Korea
[2] Electric Machine and Drive System Research Center, Korea Electrotechnology Research Institute, Changwon 51543, Korea
* Correspondence: dkhong@keri.re.kr; Tel.: +82-(0)10-9601-9234

Abstract: This paper presents a 10 kW, 12-slot 10-pole surface-mounted permanent magnet synchronous motor (SPMSM) design with fractional-slot concentrated winding for a podded propulsion system. Its load is a propeller that is proportional to the square of the rotational speed and the fifth power of the propeller diameter. Taking this into account, three SPMSMs with rated rotational speeds of 600, 1200, and 1800 rpm with the same rated output power of 10 kW were analyzed. These were designed under the same conditions (i.e., torque per rotor volume, air-gap length, current density, power factor, fill-factor, and supply voltage). Based on the SPMSMs designed by electromagnetic analysis, the housing of a podded propulsor for each SPMSM was modeled for mechanical analysis, including such parameters as forced vibration, radiated noise, and modal acoustics analysis in air and water. From the modal acoustics analysis, it is confirmed that the natural frequencies of a structure in water are lower than those in air because of the added mass effect of water.

Keywords: surface-mounted permanent magnet synchronous motor; podded propulsion; underwater radiated noise (URN); modal acoustic considering fluid-structure interaction (FSI)

Citation: Park, J.-H.; Lee, T.-W.; Jeong, Y.-H.; Hong, D.-K. Novel Multi-Physics Computational Simulation of a 10 kW Permanent Magnet Motor for Podded Propulsion. *Energies* **2022**, *15*, 6607. https://doi.org/10.3390/en15186607

Academic Editor: Frede Blaabjerg

Received: 16 August 2022
Accepted: 7 September 2022
Published: 9 September 2022

1. Introduction

Globally, a variety of regulations to reduce greenhouse gas (GHG) emissions have been continually implemented because the GHG emissions are causing climate change. The International Maritime Organization (IMO) declared in April 2018 its intention to reduce the annual GHG emissions from international shipping by 50% by 2050, relative to the emission in 2008 (taken as 100%) [1]. There are strategies to achieve these aims that improve energy efficiency, strengthen the energy efficiency design index (EEDI), and reduce the carbon intensity of new ships.

Ships that are eco-friendly include those that use liquified natural gas (LNG) fuel, hydrogen fuel, sustainable biofuel, and electric propulsion ships. Among them, an electric propulsion ship utilizes an electric motor with relatively higher efficiency, lower vibration, and lower noise compared to a ship with a conventional internal combustion [2]. Underwater radiated noise (URN) generated from a ship causes a significant impact on marine mammals [3,4]. What this means is that an electric propulsion ship with low URN can minimize damage to marine mammals. In addition, it can provide more comfort to the crews on ships and reduce detection by naval sonar.

This paper is focused on application of an electric motor for podded propulsion under the hull of a small boat or yacht. Therefore, the term "boat" is used rather than ship to avoid the perception that this might be a large boat. The concept of electric propulsion drive systems can be understood from the schematic in Figure 1. As seen in Figure 1a, the electric motor of an inboard drive is installed inside the boat. On the other hand, those with outboard and podded drives are installed outside the boat and submerged in the water, as shown in Figure 1b,c. Therefore, these drives are cooled by water, which means that a submerged electric motor can be designed with high current density.

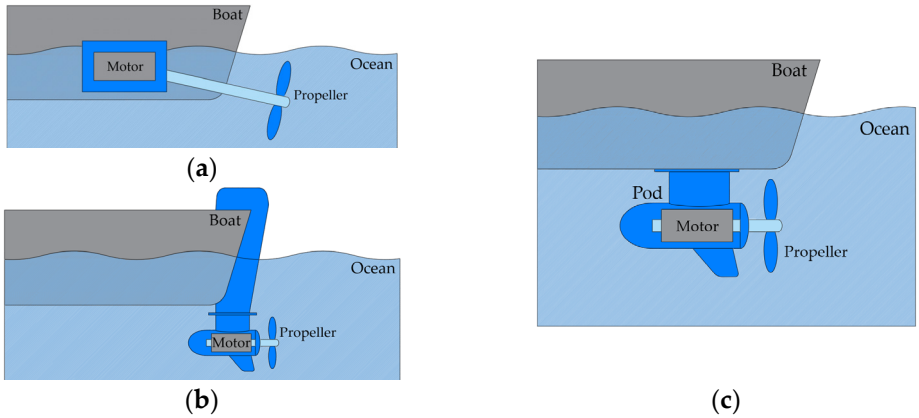

Figure 1. Schematic of electric propulsion drive systems: (**a**) inboard drive, (**b**) outboard drive, and (**c**) podded drive.

Electric motors for marine propulsion applications are classified as direct current (dc) commutator motors, induction motors, wound field synchronous motors, permanent magnet synchronous motors, and superconducting synchronous motors [5,6]. Among these types, superconducting synchronous motors have the highest torque density, but these currently need higher reliability (by preventing quench) and lower cost for practical applications. Instead of these, permanent magnet synchronous motors (PMSMs) are suitable for marine propulsion applications to realize high torque density and high efficiency within a small volume.

Generally, PMSMs are classified into interior-mounted PM (IPM) and surface-mounted PM (SPM) types. For a flux-weakening control in the constant power operation region, an IPM-type is more advantageous than an SPM-type. Additionally, its structure prevents the scattering of magnets caused by centrifugal force and electromagnetic force between the stator and the rotor. Depending on the design method, the IPM-type may have a higher torque density than the SPM-type, but the SPM-type generally has a higher torque density [7–10]. Although an SPM-type has the potential for scattering of magnets, there is an alternative method that prevents it. This problem can be solved by wrapping the magnets with carbon fiber-reinforced polymer (CFRP) as a sleeve [11,12]. Additionally, this can reduce the inertia of the rotor.

The vibration and noise of permanent magnet (PM) machines can be classified as having electromagnetic, mechanical, and aerodynamic sources. Among them, electromagnetic sources are the main sources of vibration and noise in machines that have low- to medium-rated power. The main cause of vibration and noise is radial electromagnetic force, not torque ripple or cogging torque [13]. The vibration and noise of IPM-type motors due to electromagnetic force are higher than those of an SPM-type [14].

Electric motors for marine propulsion are usually operated within the rated rotational speed, which means that the SPM-type is more suitable for such applications [7]. Therefore, to realize greater high-torque density and lower vibration and noise, a surface-mounted permanent magnet synchronous motor (SPMSM) was selected for podded propulsion in this paper.

The slot-pole combination utilized was a 12-slot 10-pole SPMSM with fractional-slot concentrated winding (FSCW). Maritime mobility applications need fault tolerance. The FSCW exhibits fault tolerance because of the non-overlapped coils [10]. A 12-slot 10-pole combination has a relatively higher winding factor than other FSCW combinations. Besides, it can be considered with a six-phase winding. Although a motor is designed with a three-phase winding, a six-phase winding can be configured by only changing the winding connection.

The load of an electric motor for podded propulsion is a propeller. The load as torque can be expressed as follows [15]:

$$T = C_T \rho {n_m}^2 D^5 \quad (1)$$

where T is the torque, C_T is the torque coefficient, ρ is the fluid density, n_m is the rotational speed, and D is the propeller diameter. The torque is proportional to the square of the rotational speed and the 5th power of the propeller diameter. Moreover, the payload and thrust force of a boat must be considered when designing its propeller. Taking this into account, this paper proposes and compares three types of 10 kW SPMSMs with rated rotational speeds of 600, 1200, and 1800 rpm. As mentioned above, the selected drive system was the podded propulsion drive shown in Figure 1c. Podded propulsion has the benefits of reduced shaft length, maneuverability, low noise and vibration, and improved propulsion efficiency from 10 to 15% [6,16]. The same conditions were selected to design all of the SPMSMs, including parameters such as torque per rotor volume (TRV), air-gap length, current density, power factor, fill factor, and supply voltage. After that, comparison of the electromagnetic characteristics of each SPMSM was carried out.

As mentioned earlier, URN is a major issue in maritime vessels. Therefore, URN analysis based on forced vibration in the stator and housing of a podded propulsor was carried out. Previous studies [17,18] reported that the natural frequencies of a structure in water are lower than those in air because of the added mass effect of water on the structure. Therefore, in order to obtain the natural frequencies of a podded propulsor with the newly designed SPMSMs, modal acoustics analysis was carried out in the water and compared with the natural frequencies in air. It should be noted that this paper is the first study to deal with modal acoustics analysis of a podded propulsor.

2. Specifications and Design Results of a 10 kW SPMSM for Podded Propulsion

The specifications with the same conditions are presented in Table 1. Every model has three-phase winding with the wye (Y) configuration. The same conditions are more focused on electromagnetic constraints than mechanical constraints. With this approach, it can be found how much the size of each model is changed. The finite element analysis (FEA) was conducted using ANSYS Electronics Desktop 2021 R2 and ANSYS Motor CAD 2021 R1.

Table 1. Design specifications for 10 kW SPMSMs.

Description		Model A *	Model B *	Model C *
Rated output power [kW]			10	
Rated rotational speed [rpm]		600	1200	1800
Rated torque [Nm]		159.15	79.57	53.05
Supply voltage [V_{dc}]			48	
Current density [A_{rms}/mm^2]			7.6	
Power factor			0.93	
TRV [kNm/m^3]			68	
Air-gap length [mm]			0.8	
Fill-factor [%]			41	
Torque ripple [%]			≤1.0	
Material	Core		35PN360 (0.35 mm)	
	PM		NdFe–N42UH (1.247 T at 60 °C)	
	Winding		Copper–AWG 18 (ϕ 1.08 mm)	

* Each model has different rated rotational speed and torque.

First, Model C was designed with a rated output power of 10 kW and rotational speed of 1800 rpm. After that, both Model A and B were designed under the same conditions based on the design result of Model C. When determining the length of the outer diameter

and the stack length of the rotor, the torque per unit rotor volume (TRV) which is related to the airgap shear stress and split ratio (SR) were used [19,20]:

$$TRV = \frac{T_{rated}}{\frac{\pi}{4} D_r{}^2 L_{stk}} \tag{2}$$

$$SR = \frac{L_{stk}}{D_r} \tag{3}$$

where, D_r is the outer diameter of the rotor, L_{stk} is the stack length, and T_{rated} is the rated output torque. In earlier work [19], it was reported that, for a large liquid-cooled machine, a TRV of 100–250 kNm/m^3 is appropriate. Therefore, an electric motor for a podded propulsor operated in water can be designed with such a TRV value. Although the TRV is an important variable to determine the rotor volume, SR is also important from the mechanical point of view. Generally, an SR between 0.5 and 2.0 is selected considering the inertia and the mechanical stresses of the rotor [20]. An electric motor with a small outer diameter is preferred for the design of a podded propulsor because, with an increase in the motor diameter, the hydraulic efficiency decreases. Therefore, SR above 2.0 was considered appropriate for the proposed models.

A current density of 10–30 A_{rms}/mm^2 is considered for liquid-cooled electric motors [19]. Although high current density is possible when making a compact electric motor, a lower value than that is considered in relation to unexpected thermal instability events. Therefore, for thermal stability, a value the same as the current density was used instead of the rated current.

Low power factor causes not only lower efficiency of the inverter system, but at the same time, it increases greater inverter capacity. Therefore, in order to match the inverter capacity, a power factor of 0.93 (which was determined in Model C) was chosen for the same condition. The air-gap length of 0.8 mm and fill-factor of 41% were selected because a smaller air-gap length and a higher fill-factor make manufacturing more difficult. A sinusoidal current was used in the electromagnetic analysis to design the proposed motors; thus, the torque-ripple target was under 1.0%.

The core material selected (35PN360) was 0.35 mm thick and was produced by POSCO (Korea). To realize high torque density, N42UH, which is a neodymium-iron-boron permanent magnet, was used. The residual flux density of N42UH is 1.35 T at 20 °C. However, its value of 1.247 at 60 °C was selected considering the design margins and change of the magnet temperature during operation. To reduce the PM eddy current loss, the PMs were divided into four segments in the axial direction as shown in Figure 2.

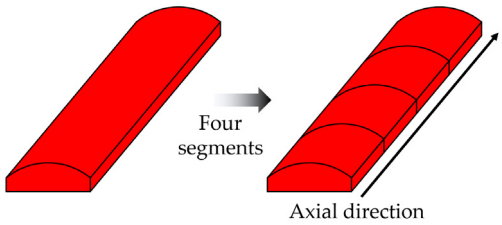

Figure 2. Segmented PMs.

The three types of 10 kW SPMSMs proposed for the podded propulsion system are shown in Figure 3, and Table 2 indicates the design results for the main dimensions and electromagnetic analysis results. All of the required electromagnetic characteristics specified in Table 1 were satisfied. The SR of Model C is 2.26, but in Model A and B, the SR was increased by 13.7% and 7.1%, respectively, because only the extension of the stack length increases resistance of the winding which leads to an increase in the copper loss.

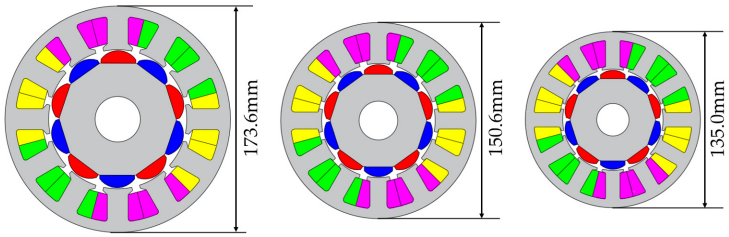

Figure 3. Newly designed 10 kW SPMSMs: (**a**) Model A, (**b**) Model B, (**c**) Model C.

Table 2. Design results for the new 10 kW SPMSMs.

Description		Model A	Model B	Model C
Rated output power [kW]		10.01	10.15	10.03
Rated rotational speed [rpm]		600	1200	1800
Rated torque [Nm]		159.35	80.81	53.22
Current density [A_{rms}/mm^2]		7.66	7.59	7.63
Power factor		0.931	0.930	0.930
TRV [kNm/m^3]		68.67	68.87	68.21
Torque ripple [%]		0.90	0.54	0.94
SR		2.57	2.42	2.26
Rated current [A_{rms}]		227	225	201
Efficiency [%]		90.20	93.17	94.37
Total loss [%]		1081.84	744.4	598.6
Losses [W]	Copper	969.5	610.3	443.3
	PM	9.34	14.8	12.4
	Iron	53.0	69.3	92.9
	Mechanical *	50	50	50
Outer diameter of stator [mm]		173.6	150.6	135
Inner diameter of stator [mm]		106.6	87.6	77.6
Outer diameter of rotor [mm]		105	86	76
Thickness of stator yoke [mm]		8	7.5	6.5
Stack length [mm]		268	202	172
The number of turns per slot		6	5	5
The number of strands per turn		18	18	16
Parallel branch		2	2	2
Resistance per phase [ohm]		0.006271	0.004018	0.003657
Active volume of motor [m^3]		0.00639	0.00363	0.00246
Active weight of motor [kg]		41.40	23.43	15.85

* Assumed 0.5% of output power.

The electrical loading differs according to the current rating, number of turns per slot, and strands per turn. In Model A, the number of turns per slot was increased by 1, compared with the other models, to achieve the required rated torque with the restricted voltage supply. Because their current densities were considered the same, the rated currents and the number of strands per turn of Model A and B were a little higher than those of Model C. Generally, torque is proportional to the diameter of the rotor. Therefore, to increase torque at the same output power, the diameter of the rotor increases with an increased outer diameter of stator which leads to the increased resistance of winding. As a results, Model A has the lowest efficiency.

The motor weight includes the motor core, winding, and PM. The results show that the weights of Model A and B are higher by 261.2% and 147.8%, respectively, compared to Model C. Moreover, the volumes of Model A and B are greater by 259.7% and 147.5% compared to Model C. These results show that the weight and the volume were increased to realize a low-speed, high-torque electric motor.

Figure 4 shows the torque-speed curves of the three types of 10 kW SPMSMs. As seen in the figure, a 10 kW podded propulsor (Model A) with low speed and high torque can

be used to turn a large-diameter propeller. In contrast, Model C, with high speed and low torque, is better suited to turn a small-diameter propeller.

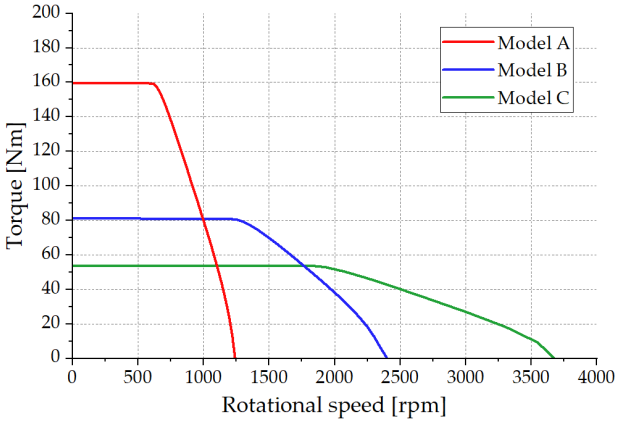

Figure 4. Torque-speed curves of the 10 kW SPMSMs.

The flux density of the newly designed models at the rated point is shown in Figure 5. The scale of flux density set was 0.00 to 1.80 T. This was because the saturated level of 35PN360 is almost 1.80 T. As it is shown in Figure 5 below, the saturation of the flux density on the stator teeth is generated, but it is within acceptable range.

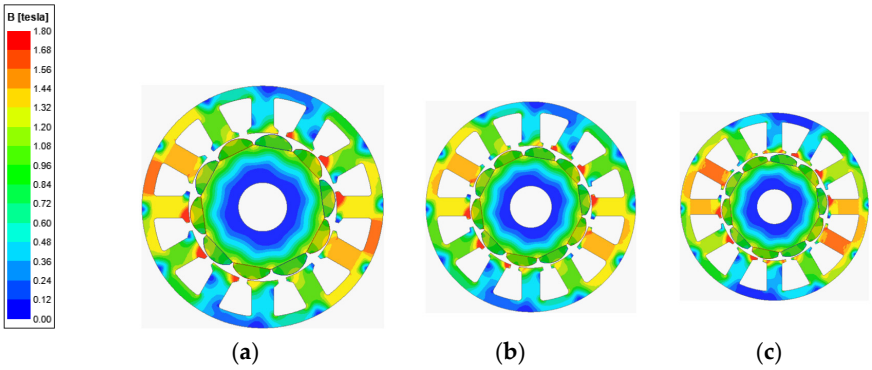

Figure 5. Flux density of the new 10 kW SPMSMs: (**a**) Model A, (**b**) Model B, (**c**) Model C.

Figure 6 shows the efficiency maps for the newly designed models. The overall contours of the efficiency maps are high in terms of an assumed propeller load curve which can be calculated from Equation (1).

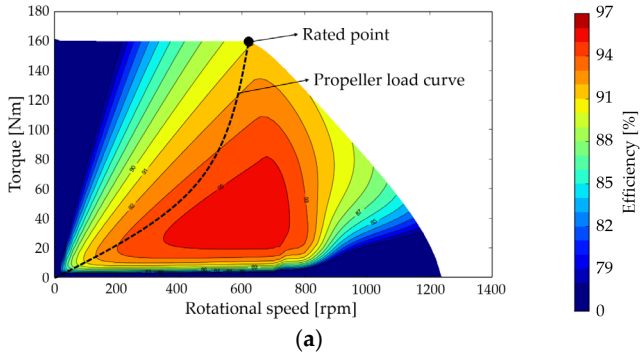

(**a**)

Figure 6. *Cont.*

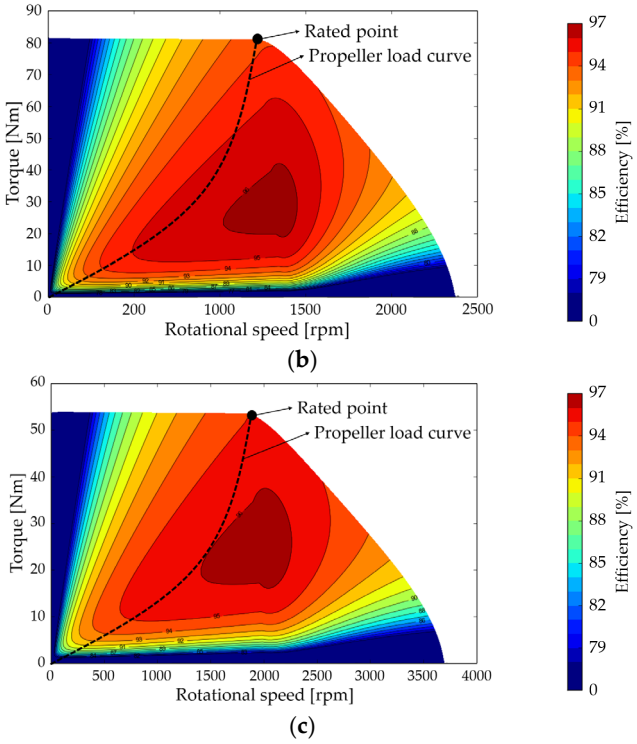

Figure 6. Efficiency maps of the new 10 kW SPMSMs: (**a**) Model A, (**b**) Model B, (**c**) Model C.

3. Mechanical Analysis of the 10 kW SPMSMs for Podded Propulsion

3.1. Podded Propulsor for Mechanical Analysis

The podded propulsor for each 10 kW SPMSM is presented in Figure 7. For simple analysis, the propeller part was not considered in this paper. Each podded propulsor contains the SPMSM design, housing, shaft, and two bearings. A point mass on the stator teeth, instead of modeled winding, was applied because it is difficult to consider the exact contact condition between the stator and the winding. Based on the schematic of the podded propulsor shown in Figure 1c, the fixed support condition for mechanical analysis was considered the upper part of the podded propulsor. The mechanical analysis utilized material properties that are listed in Table 3. The FEA was conducted using ANSYS Mechanical 2021 R2.

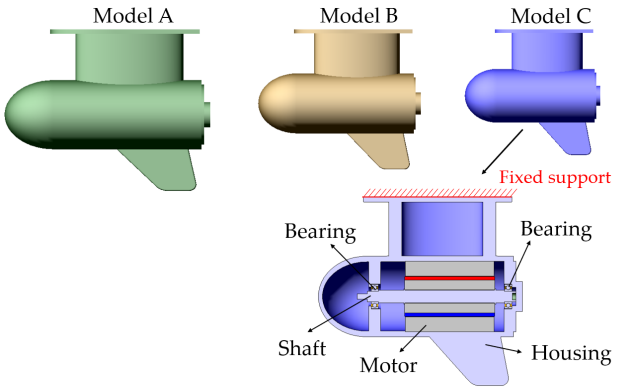

Figure 7. Podded propulsors for the 10 kW SPMSMs.

Table 3. Material properties used in the mechanical analysis.

Description	**Housing**	**Structure**		
		Core	**Motor PM**	**Shaft**
Material	Aluminum	35PN360	N42UH	SUS304
Density [kg/m^3]	2810	7600	7650	8000
Young's modulus [GPa]	71.7	195	153	193
Poisson's ratio	0.33	0.25	0.24	0.285
Description	**Fluid**			
Material	Air		Water	
Density [kg/m^3]	1.225		998.2	
Speed of sound [m/s]	346.2		1482.1	

3.2. Modal Acoustic Analysis Considering Fluid-Structure Interaction (FSI)

For modal acoustic analysis in a fluid, the fluid-structure interaction (FSI), which is the coupled interaction behavior between a fluid flow and a solid structure, must be considered. The equations of motion of the structure and fluid [21] can be expressed as:

$$\begin{bmatrix} [M_s] & 0 \\ \overline{\rho}_0[R]^T & [M_f] \end{bmatrix} \begin{Bmatrix} \{\ddot{u}\} \\ \{\ddot{p}\} \end{Bmatrix} + \begin{bmatrix} [C_S] & 0 \\ 0 & [C_f] \end{bmatrix} \begin{Bmatrix} \{\dot{u}\} \\ \{\dot{p}\} \end{Bmatrix} + \begin{bmatrix} [K_S] & -[R] \\ 0 & [K_f] \end{bmatrix} \begin{Bmatrix} \{u\} \\ \{p\} \end{Bmatrix} = \begin{Bmatrix} \{F_s\} \\ \{F_f\} \end{Bmatrix} \quad (4)$$

where, $\{u\}$ is the node displacement vector, $[M_s]$, $[C_S]$, and $[K_S]$ are the mass matrix, the damping matrix, and the stiffness matrix of the structure, and $\{F_s\}$ is the load applied to the structure. Here, $\{p\}$ is the node pressure; $[M_f]$, $[C_f]$, and $[K_f]$ are the mass matrix, the damping matrix, and the stiffness matrix of the fluid. The term $\overline{\rho}_0$ is the acoustic fluid mass density constant, $\{F_f\}$ is the load applied to the fluid, and $[R]$ is the acoustic fluid boundary matrix between the fluid and the structure, which is defined as:

$$[R] = \int_s \{N_u\}\{N_p\}^T\{n\}dS \quad (5)$$

where $\{N_u\}$ is the element shape function for displacements, $\{N_p\}$ is the element shape function for pressure, and $\{n\}$ is the outward normal vector at the fluid boundary. S is the surface. From Equation (4), it indicates that the FSI depends on the mass and stiffness terms except for the damping. From Equation (5), it is recommended that the nodes of the structure be in contact with the nodes of the fluid for the FSI interface.

To obtain the natural frequencies, the damping matrix term and the loads can be neglected; then, Equation (4) can be expressed as:

$$\begin{bmatrix} [M_s] & 0 \\ \overline{\rho}_0[R]^T & [M_f] \end{bmatrix} \begin{Bmatrix} \{\ddot{u}\} \\ \{\ddot{p}\} \end{Bmatrix} + \begin{bmatrix} [K_S] & -[R] \\ 0 & [K_f] \end{bmatrix} \begin{Bmatrix} \{u\} \\ \{p\} \end{Bmatrix} = \begin{Bmatrix} 0 \\ 0 \end{Bmatrix} \quad (6)$$

Equation (6) in the time domain is transformed to the frequency domain as follows:

$$\begin{bmatrix} \{-[M_s]\omega^2 + [K_S]\} & -[R] \\ -\overline{\rho}_0[R]^T\omega^2 & -[M_f]\omega^2 + [K_f] \end{bmatrix} \begin{Bmatrix} \{u\} \\ \{p\} \end{Bmatrix} = \begin{Bmatrix} 0 \\ 0 \end{Bmatrix} \quad (7)$$

When Equation (7) is changed to the structural part with fluid effect, then it can be expressed as:

$$\left[\left\{-[M_s] - \overline{\rho}_0[R]\{-[M_f]\omega^2 + [K_f]\}^{-1}[R]^T\right\}\omega^2 + [K_S]\right]\{u\} = 0 \quad (8)$$

For air conditions, both $[M_f]$ and $[K_f]$ can be neglected because these effects are very small; then, Equation (8) can be expressed as:

$$[-[M_s]\omega^2 + [K_S]]\{u\} = 0 \quad (9)$$

Unlike with Equation (9), Equation (8) has the term $\overline{\rho}_0[R]\{-[M_f]\omega^2 + [K_f]\}^{-1}[R]^T$, which is related directly to the added mass effect of water on the structure.

Figure 8 shows the finite element model of the podded propulsor used for the modal acoustics analysis of Model C, which was the same for the other models. The FSI interface applies to the structure with the fluid, and the nodes of the structure were in contact with the fluid. For boundary conditions, a sphere absorbing element boundary condition that involved an infinite, homogenous, and inviscid fluid, was selected because the podded propulsor is submerged in seawater or river water [21].

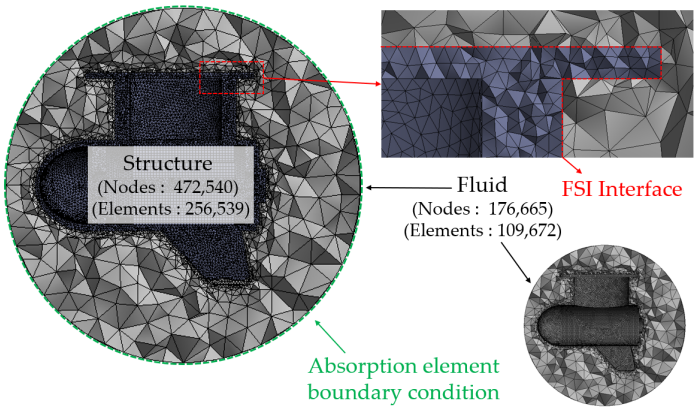

Figure 8. Finite element model of the podded propulsor for Model C.

The modal acoustic analysis results by FEA (in air and water) for each podded propulsor are indicated in Table 4. It is obvious that the natural frequencies of podded propulsors in water are lower than those in air. This is due to the added mass effect of water because the density of water is much higher than that of air (as specified in Table 3). Generally, the natural frequencies decrease when the mass of a structure increases. Therefore, the natural frequencies of Model C, which has the lowest mass and volume, are higher than those of the other models.

Table 4. Modal acoustic analysis results in air and in water.

Description		Model A	Model B	Model C
1st natural frequency [Hz] (bending mode)	in air	172.17	213.43	239.52
	in water	154.98	189.18	212.58
2nd natural frequency [Hz] (bending mode)	in air	494.06	590.71	629.18
	in water	475.93	558.86	601.80
3rd natural frequency [Hz] (bending mode)	in air	925.53	1097.40	1209.10
	in water	823.67	981.53	1092.90

It is noteworthy that the mode shapes in water were not changed, compared to those in air, as presented in Figure 9. Each mode has the bending mode, but its direction is different. It is the direction of vibration that is generated when an operating frequency is close to or equal to the natural frequency. The deformation of mode shapes was generated for the housing with the stator in 1st and 2nd mode; whereas, the rotor vibration mode was generated in the 3rd mode. This has effects on the housing that cause deformation of the housing and the stator.

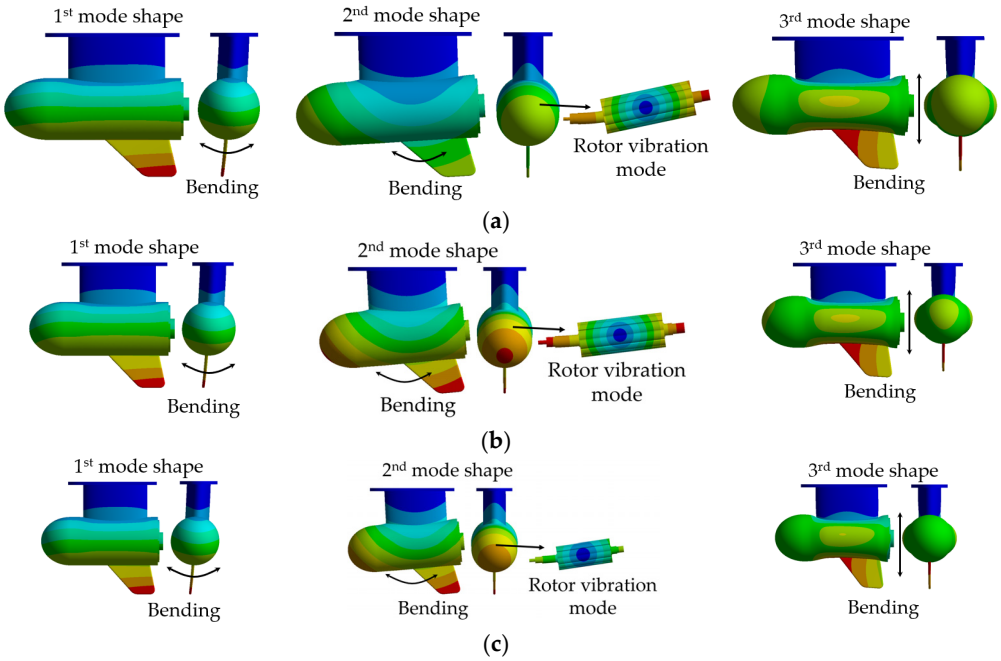

Figure 9. Mode shapes of the podded propulsors in air: (**a**) Model A, (**b**) Model B, (**c**) Model C.

3.3. Forced Vibration and Underwater Radiated Noise Analysis

Forced vibration and underwater radiated noise analysis of the podded propulsors were conducted based on electromagnetic force. A flowchart of the analysis is presented in Figure 10.

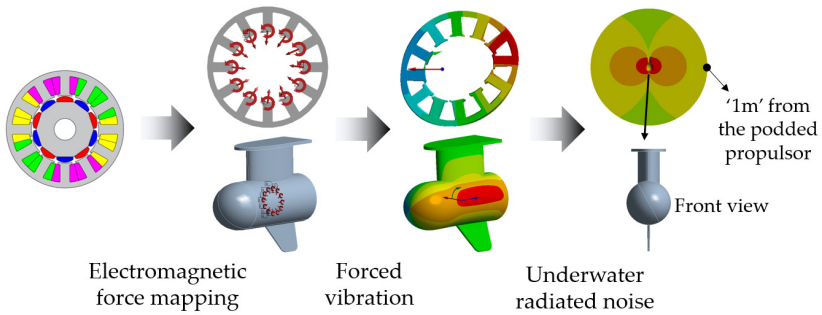

Figure 10. Flowchart of the forced vibration and underwater radiated noise analyses.

The radial electromagnetic force density F_r can be calculated using a Maxwell stress tensor method as follows [22]:

$$F_r = \frac{1}{2\mu_0}\left({B_r}^2 - {B_t}^2\right) \tag{10}$$

where $\mu_0 \approx 4\pi \times 10^{-7}$ is the magnetic permeability of free space (air or vacuum). B_r and B_t are the radial flux density and tangential flux density in the air-gap. The unit of the radial electromagnetic force density is Newton/square meter which equals to pascal (symbol: Pa). Figure 11 shows the radial electromagnetic force density in the air-gap at a single point calculated from the air-gap flux density on the load as shown in Figure 12. The radial electromagnetic force density of each model shows the difference, but it is not significant.

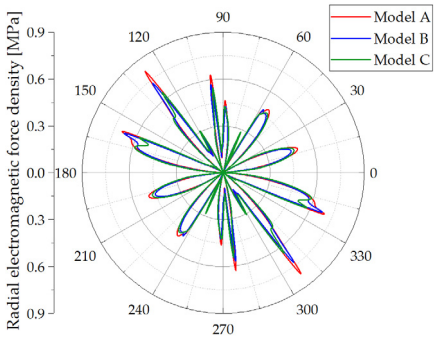

Figure 11. Radial electromagnetic force density in air-gap.

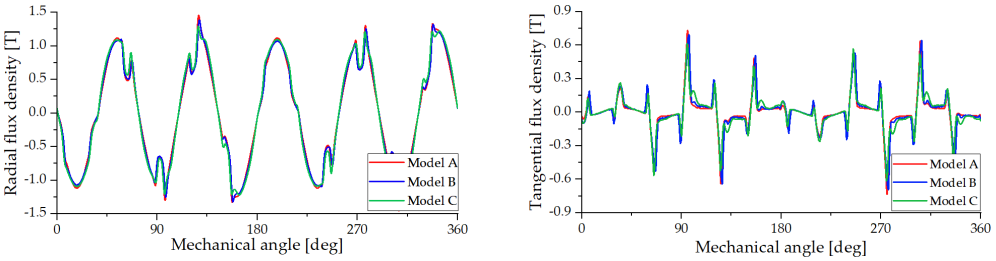

(**a**) (**b**)

Figure 12. Air-gap flux density on load: (**a**) Radial flux density, (**b**) Tangential flux density.

An environmental temperature of 22 °C was considered and the URN level was measured 1 m from the noise source [23,24]. Therefore, the boundary region for analysis was determined using this distance. In common with modal acoustics analysis, the sphere absorbing element boundary condition was considered in the acoustic analysis. The electrical frequency of an electric motor f_e is calculated as follows:

$$f_e = \frac{n_m p}{60} \tag{11}$$

where n_m is the rotational speed; p is the number of poles. A pole-passing frequency f_{pp} related with an excitation frequency is calculated as follows:

$$f_{pp} = 2 \times f_e \tag{12}$$

The sound pressure level L_{SPL} can be calculated as follows [25]:

$$L_{SPL} = 20log_{10}\left(\frac{P_{rms}}{P_o}\right) = 10log_{10}\left(\frac{W}{W_0}\right) - 10log_{10}\left(\frac{A}{A_0}\right) \tag{13}$$

where P_{rms} is the root mean square sound pressure and P_o is the reference sound pressure. P_o of air is 20 µPa, whereas for water it is 1 µPa. The term W is the sound power, W_0 is the reference sound power (10^{-12} W), A is the radiating surface area, and A_0 is the reference radiating surface area (1 m^2). For acoustic analysis, the boundary of a sphere was selected, and thus A is 4 πr^2, where r is the distance from the source. Here, the sound power of an electric machine W_m can be calculated as follows [13]:

$$W_m = 2\sigma_{rel}\rho c\pi^3 f_{pp}^2 x^2 D_s L_{stk} \tag{14}$$

where, $\sigma_{rel} = k^2/1 + k^2$, $k = \pi D_s f_{pp}/c$, c is the speed of sound, x is the radial displacement, and D_s is the outer diameter of the stator.

Table 5 indicates the vibration response displacement and radiated noise analysis results at the rated output power. It is confirmed that the URN in water is higher than in air. The contour of vibration response displacement and radiated noise are presented in

Figures 13 and 14. For radiated noise analysis, the fluid boundary region for the sound field is built expecting the modeled podded propulsor. The analysis results of Model B show that the vibration response displacement is the highest value, and thus its radiated noise calculated at 1 m distance is also higher than those of the other models. This is because the 1st natural frequency of Model B (indicated in Table 4) is close to its pole-passing frequency, which means it is near the resonance point.

Table 5. Vibration response displacement and radiated noise analysis results.

Description		Model A	Model B	Model C
Rated rotational speed [rpm]		600	1200	1800
Electrical frequency, f_e [Hz]		50	100	150
Pole-passing frequency, f_{pp} [Hz]		100	200	300
Max. vibration response displacement [μm]		7.40	22.89	4.14
Max. radiated noise at 1 m [dB]	in air	54.49	78.40	70.80
	in water (URN)	132.22	159.66	140.35

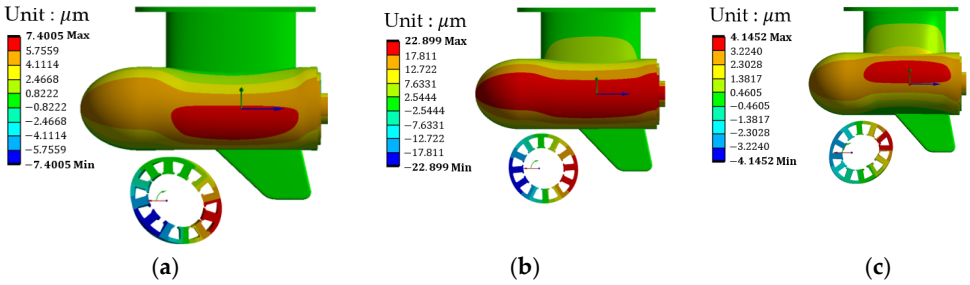

Figure 13. Vibration response displacement: (**a**) Model A, (**b**) Model B, (**c**) Model C.

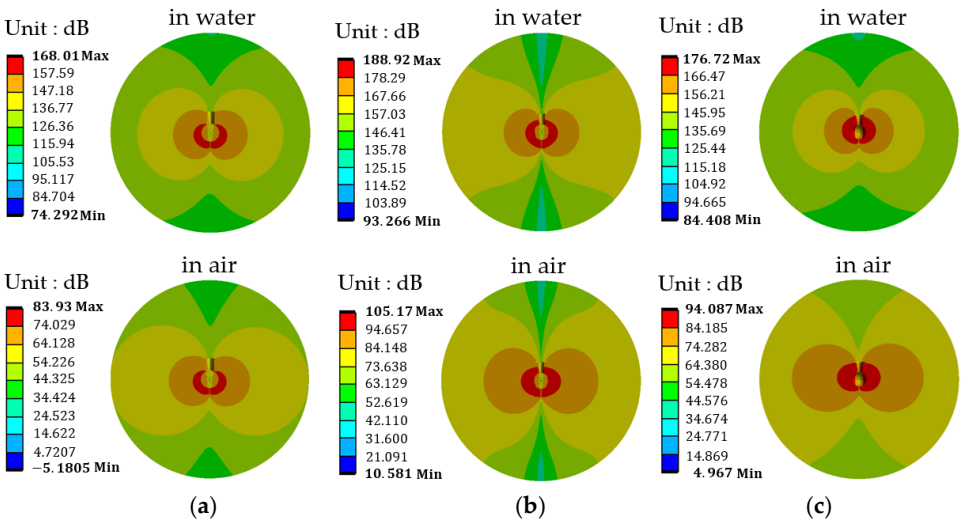

Figure 14. Radiated noise: (**a**) Model A, (**b**) Model B, (**c**) Model C.

The vibration response displacement of Model A is higher than that of Model C, but the radiated noise of Model A is lower than that of Model C. There are various causes of this difference. First, is the different distribution of the vibration response displacement shown in Figure 13a,c. Second, the distribution of the vibration response velocity for radiated noise analysis generated by forced vibration is also different, as shown in Figure 15a,c. Moreover, the sound power is proportional to the square of the pole-passing frequency in Equation (14). The pole-passing frequency of Model C is three times that of Model A. As a result, it can be estimated that the radiated noise level of Model C is higher than that of Model A.

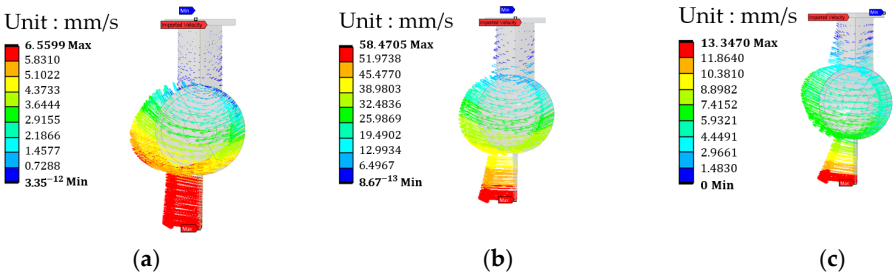

(**a**) (**b**) (**c**)

Figure 15. Vibration response velocity: (**a**) Model A, (**b**) Model B, (**c**) Model C.

4. Conclusions

In this paper, three types of 10 kW SPMSMs for a podded propulsor are presented. The SPMSMs were designed under the same conditions and based on electromagnetic analysis. With the newly designed SPMSMs, it was observed that, to realize high torque with restricted output power requires a large motor volume and weight. The mechanical analysis, which includes forced vibration, radiated noise, and a modal acoustic analysis in air and water, was carried out on each SPMSM with a modeled podded propulsor. For modal acoustic analysis considering FSI, the natural frequencies of the podded propulsor decreased due to the added mass effect of water in comparison with that of air. If the design requires resonance avoidance, modal acoustic analysis to obtain a natural frequency in water for an electric propulsion system, such as a podded propulsor or an outboard propulsor, must be required. The necessity for design of resonance avoidance was confirmed with Model B because its pole-passing frequency is close to the 1st natural frequency, and thus a higher vibration response and radiated noise is generated than with the other models. In the future, validation tests of the simulation and experimental results for one of the proposed 10 kW SPMSMs for a podded propulsor will be conducted. Moreover, the comparison of natural frequencies in air and water will be also conducted for the fabricated propulsor.

Author Contributions: Conceptualization, J.-H.P. and D.-K.H.; software, J.-H.P. and Y.-H.J.; validation, J.-H.P., T.-W.L., Y.-H.J. and D.-K.H.; investigation, J.-H.P., T.-W.L. and Y.-H.J.; writing—original draft preparation, J.-H.P.; writing—review and editing, J.-H.P. and T.-W.L.; visualization, J.-H.P.; supervision, D.-K.H.; project administration, D.-K.H. All authors have read and agreed to the published version of the manuscript.

Funding: This research was supported by Korea Electrotechnology Research Institute (KERI) Primary research program through the National Research Council of Science & Technology (NST) funded by the Ministry of Science and ICT (MSIT) (No. 22A01015).

Data Availability Statement: Some or all of the data and the models generated or used during the study, are available in a repository or online.

Acknowledgments: This project was conducted with KERI.

Conflicts of Interest: The authors declare no conflict of interest.

References

1. Joung, T.H.; Kang, S.G.; Lee, J.K.; Ahn, J. The IMO initial strategy for reducing Greenhouse Gas (GHG) emissions, and its follow-up actions towards 2050. *J. Int. Marit. Saf. Environ. Aff. Shipp.* **2020**, *4*, 1–7. [CrossRef]
2. Litwin, W.; Leśniewski, W.; Piątek, D.; Niklas, K. Experimental Research on the Energy Efficiency of a Parallel Hybrid Drive for an Inland Ship. *Energies* **2019**, *12*, 1675. [CrossRef]
3. Erbe, C.; Marley, S.A.; Schoeman, R.P.; Smith, J.N.; Trigg, L.E.; Embling, C.B. The effects of ship noise on marine mammals—A review. *Front. Mar. Sci.* **2019**, *6*, 606. [CrossRef]
4. Williams, R.; Wright, A.J.; Ashe, E.; Blight, L.K.; Bruintjes, R.; Canessa, R.; Clark, C.W.; Cullis-Suzuki, S.; Dakin, D.T.; Erbe, C.; et al. Impacts of anthropogenic noise on marine life: Publication patterns, new discoveries, and future directions in research and management. *Ocean Coast. Man.* **2015**, *115*, 17–24. [CrossRef]
5. Kirtley, J.L.; Banerjee, A.; Englebretson, S. Motors for Ship Propulsion. *Proc. IEEE* **2015**, *103*, 2320–2332. [CrossRef]

6. Bassham, B.A. An Evaluation of Electric Motors for Ship Propulsion. Ph.D. Thesis, Naval Postgraduate School, Monterey, CA, USA, 2003.
7. Bianchi, N.; Bolognani, S.; Ruzojcic, B. Design of a 1000 HP Permanent Maget Synchronous Motor for Ship Propulsion. In Proceedings of the 2009 13th European Conference on Power Electronics and Applications, Barcelona, Spain, 8–10 September 2009; pp. 1–8.
8. Ocak, O.; Aydin, M. A New Hybrid Permanent Magnet Synchronous Motor with Two Different Rotor Sections. *IEEE Trans. Magn.* **2017**, *53*, 1–5. [CrossRef]
9. Hwang, C.C.; Chang, C.M.; Cheng, S.P.; Chan, C.K.; Pan, C.T.; Chang, T.Y. Comparison of Performances between IPM and SPM Motors with Rotor Eccentricity. *J. Magn. Magn. Mater.* **2004**, *282*, 360–363. [CrossRef]
10. Barcaro, M.; Bianchi, N.; Magnussen, F. Analysis and Tests of a Dual Three-Phase 12-Slot 10-Pole Permanent-Magnet Motor. *IEEE Trans. Ind. Appl.* **2010**, *46*, 2355–2362. [CrossRef]
11. Brecher, C.; Schug, R.; Schmitz, S.; Börner, U. Design and Manufacture of a Carbon Fibre Spindle Rotor Project Results "Aerospin—Development of a Highly Precise Spindle Prototype". *Sci. Eng. Compos. Mater.* **2007**, *14*, 219–228. [CrossRef]
12. Lee, T.-W.; Hong, D.-K. Rotor Design, Analysis and Experimental Validation of a High-Speed Permanent Magnet Synchronous Motor for Electric Turbocharger. *IEEE Access* **2022**, *10*, 21955–21969. [CrossRef]
13. Islam, R.; Husain, I. Analytical Model for Predicting Noise and Vibration in Permanent-Magnet Synchronous Motors. *IEEE Trans. Ind. Appl.* **2010**, *46*, 2346–2354. [CrossRef]
14. Ko, H.-S.; Kim, K.-J. Characterization of Noise and Vibration Sources in Interior Permanent-Magnet Brushless DC Motors. *IEEE Trans. Magn.* **2004**, *40*, 3482–3489. [CrossRef]
15. Esmailian, E.; Ghassemi, H.; Zakerdoost, H. Systematic Probabilistic Design Methodology for Simultaneously Optimizing the Ship Hull–Propeller System. *Int. J. Nav. Archit. Ocean Eng.* **2017**, *9*, 246–255. [CrossRef]
16. Adnanes, A.K. *Maritime Electrical Installations and Diesel Electric Propulsion*; ABB AS Marine: Oslo, Norway, 2003.
17. Rodriguez, C.G.; Egusquiza, E.; Escaler, X.; Liang, Q.W.; Avellan, F. Experimental Investigation of Added Mass Effects on a Francis Turbine Runner in Still Water. *J. Fluids Struct.* **2006**, *22*, 699–712. [CrossRef]
18. Huang, X.; Escaler, X. Added Mass Effects on a Francis Turbine Runner with Attached Blade Cavitation. *Fluids* **2019**, *4*, 107. [CrossRef]
19. Hendershot, J.R.; Miller, T.J.E. *Design of Brushless Permanent-Magnet Motors*; Oxford University Press: London, UK, 1995; pp. 88–90.
20. Kim, H.-J.; Jeong, J.-S.; Yoon, M.-H.; Moon, J.-W.; Hong, J.-P. Simple Size Determination of Permanent-Magnet Synchronous Machines. *IEEE Trans. Ind. Electron.* **2017**, *64*, 7972–7983. [CrossRef]
21. ANSYS Inc. *Mechanical APDL Theory Reference*; ANSYS: Canonsburg, PA, USA, 2022.
22. Zhu, W.; Pekarek, S.; Fahimi, B.; Deken, B.J. Investigation of Force Generation in a Permanent Magnet Synchronous Machine. *IEEE Trans. Energy Convers.* **2007**, *22*, 557–565. [CrossRef]
23. Korea Register. *Guidances for Underwater Radiated Noise*; Korea Register: Busan, Korea, 2021.
24. McKenna, M.F.; Ross, D.; Wiggins, S.M.; Hildebrand, J.A. Underwater Radiated Noise from Modern Commercial Ships. *J. Acoust. Soc. Am.* **2012**, *131*, 92–103. [CrossRef] [PubMed]
25. Norton, M.P.; Karczub, D.G. *Fundamentals of Noise and Vibration Analysis for Engineers*, 2nd ed.; Cambridge University Press: Cambridge, UK, 2003; pp. 273–274.